ARTICLE

https://doi.org/10.1038/s41467-019-08629-9 OPEN

Intrinsic valley Hall transport in atomically thin MoS_2

Zefei Wu[1], Benjamin T. Zhou[1], Xiangbin Cai[1], Patrick Cheung[2], Gui-Bin Liu[3], Meizhen Huang[1], Jiangxiazi Lin[1], Tianyi Han[1], Liheng An[1], Yuanwei Wang[1], Shuigang Xu[1], Gen Long[1], Chun Cheng[4], Kam Tuen Law[1], Fan Zhang[2] & Ning Wang[1]

Electrons hopping in two-dimensional honeycomb lattices possess a valley degree of freedom in addition to charge and spin. In the absence of inversion symmetry, these systems were predicted to exhibit opposite Hall effects for electrons from different valleys. Such valley Hall effects have been achieved only by extrinsic means, such as substrate coupling, dual gating, and light illuminating. Here we report the first observation of intrinsic valley Hall transport without any extrinsic symmetry breaking in the non-centrosymmetric monolayer and trilayer MoS_2, evidenced by considerable nonlocal resistance that scales cubically with local resistance. Such a hallmark survives even at room temperature with a valley diffusion length at micron scale. By contrast, no valley Hall signal is observed in the centrosymmetric bilayer MoS_2. Our work elucidates the topological origin of valley Hall effects and marks a significant step towards the purely electrical control of valley degree of freedom in topological valleytronics.

[1] Department of Physics and the Center for Quantum Materials, the Hong Kong University of Science and Technology, Hong Kong, China. [2] Department of Physics, University of Texas at Dallas, Richardson, TX 75080, USA. [3] School of Physics, Beijing Institute of Technology, 100081 Beijing, China. [4] Department of Materials Science and Engineering, Southern University of Science and Technology, 518055 Shenzhen, China. These authors contributed equally: Zefei Wu, Benjamin T. Zhou, Xiangbin Cai. Correspondence and requests for materials should be addressed to Z.W. (email: wzefei@connect.ust.hk) or to F.Z. (email: zhang@utdallas.edu) or to N.W. (email: phwang@ust.hk)

Electron valley degree of freedom emerges as local extrema in the electronic band structures. Inequivalent valleys, well separated in the Brillouin zone, can be energetically degenerate due to symmetry and serve as novel information carriers controllable via external fields[1–6]. A feasible means to manipulate such a valley degree of freedom is through a valley Hall effect (VHE)[5–9]. Analogous to an ordinary Hall effect, in which a transverse charge current is driven by a uniform magnetic field in real space, a transverse valley current in the VHE is produced by valley-contrasting Berry curvatures in momentum space. Upon the application of an external electric field, the curvatures drive carriers from different valleys to traverse in opposite directions. Therefore, the VHE has been a major theme in the study of valleytronics, particularly in those 2D materials featuring K and K' valleys in their hexagonal Brillouin zones[10–19].

As Berry curvature is even under spatial inversion (P) and odd under time reversal (T), the VHE cannot survive when both P and T symmetries are present. To achieve VHEs in monolayer and bilayer graphene, an elaborately aligned h-BN substrate[10] and a strong dual gating field[11,12] were respectively utilized to break the P symmetry. To excite VHEs in specific valleys[17,18], circularly polarized lights[20–22] were used for breaking the T symmetry in atomically thin transition-metal dichalcogenides (TMDC). Monolayer TMDCs have direct band gaps of optical frequencies at two inequivalent K-valleys[23,24], due to the intrinsic P asymmetry in their unit cells depicted in Fig. 1a. Thus, Berry curvatures with opposite signs naturally emerge at the two K-valleys. Moreover, the T and mirror symmetries lock the spin and valley indices of the sub-bands split by the spin-orbit couplings, both of which are flipped under T; the spin conservation suppresses the inter-valley scattering. Therefore, monolayer TMDCs have been deemed an ideal platform for realizing intrinsic VHE without extrinsic symmetry breaking[15,16].

However, the quantum transport in atomically thin TMDCs has been a long-standing challenge due to the low carrier mobility and the large contact resistance in their field-effect devices prepared by an exfoliation method. Recent breakthroughs in the fabrication of low-temperature ohmic contacts for high-mobility 2D TMDC devices[25–28] have already facilitated the observation of transport hallmarks of Q-valley electrons[28,29], K-valley electrons[30,31], K-valley holes[32–34], and Γ-valley holes[35]. These discoveries have revealed the rich and unique valley physics in the platform of atomically thin TMDCs.

In this work, we design nonlocal, layer-dependent, transport measurements to systematically examine the intrinsic VHEs in n-type 2H-MoS_2. For the first time, we observe nonlocal resistances that exhibit cubic power-law scaling with the local resistances in the monolayers and trilayers, evidencing intrinsic VHEs. Because of the large intrinsic bandgaps and spin-valley locking of TMDCs, such VHEs can even be observed at room temperature in our monolayer devices. Beyond critical carrier densities ($\sim 4.0 \times 10^{11}$ cm^{-2} for monolayers and trilayers), the cubic scaling turns into linear scaling. Notably, only linear scaling is observed in bilayer MoS_2, where the P symmetry is restored. Intriguingly, although the monolayer and trilayer feature respectively K- and Q-valleys near their conduction-band edges, they display comparable valence-band Berry curvatures, valley Hall signatures, and micron-sized valley diffusion lengths. Our results not only offer the first experimental evidence for the intrinsic VHE but also help elucidate its topological origin[6] in odd-layer TMDCs and pave the way for realizing room-temperature low-dissipation valleytronics by purely electronic means.

Results

Devices for nonlocal measurements. The structure of a monolayer MoS_2 field-effect transistor is sketched in Fig. 1b. Its bright-field cross-sectional scanning transmission electron microscopy (STEM) image in Fig. 1c clearly shows the layered BN-MoS_2-BN structure without any impurities in the interfaces down to the atomic scale. The device fabrication process includes a dry transfer step followed by a reactive ion etching step[27,28,35] (see Methods and Supplementary Fig. 1 for details). A low contact barrier formed on the n-type MoS_2 is evidenced by the I-V curves, contact resistances (Supplementary Fig. 2), and the field-effect mobilities μ varied from 500–4000 $cm^2\,V^{-1}\,s^{-1}$ for monolayers, 4000–23000 $cm^2\,V^{-1}\,s^{-1}$ for bilayers, and 10000–25000 $cm^2\,V^{-1}\,s^{-1}$ for trilayers at $T = 2$ K (Supplementary Figs. 3 and 4). The impurity-free STEM images and the high mobilities coincide well with the low residue carrier densities ($n^* = 4 \times 10^{10}\,cm^{-2}$, see Supplementary Fig. 5).

As for the electronic measurement, an inverse VHE is exploited to detect a valley current, as sketched in Fig. 1d. An applied current I_{12} through probes 1 and 2 induces charge imbalance in a remote region, as measured by the voltage drop V_{34} between probes 3 and 4 (Supplementary Fig. 6). The nonlocal resistance $R_{NL} = V_{34}/I_{12}$ mediated by the valley Hall current was predicted[36] to present cubic power-law dependence on the local resistance $R_L = V_{24}/I_{13}$.

Nonlocal transport in monolayer MoS_2. Nonlocal resistance R_{NL} in an n-type monolayer MoS_2 (sample B of length $L = 6$ μm and width $W = 1.5$ μm illustrated in the inset of Fig. 1e), measured as a function of gate voltage V_g at varied temperatures, is shown in Fig. 1e. A giant R_{NL} is observed in the range of $V_g \sim -15$ to -25 V that amounts to the electron density $n \sim 10^{10}$ to $10^{11}\,cm^{-2}$. In particular, the observed $R_{NL} \sim 10^6\,\Omega$ exceeds the classical ohmic contribution $R_{CL} = R_L \frac{W}{\pi L} e^{-\pi L/W} \sim 10^4\,\Omega$ by two orders of magnitude in the range of $V_g \sim -15$ to -18 V at 2 K and $V_g \sim -22$ to -25 V at 300 K. Another unexpected feature of R_{NL} is its V_g dependence. In sharp contrast to the classical contribution R_{CL}, which decreases gradually with increasing V_g, the observed R_{NL} drops by at least one order of magnitude within an increase of several volts in V_g. Both the pronounced nonlocal signal and its unusual sensitivity to V_g suggest that the observed R_{NL} has a physical origin different from the classical ohmic contribution R_{CL}.

The temperature dependence of R_L and R_{NL} uncovers the mesoscopic mechanism of both the local and nonlocal transport. The conduction can be separated into three regimes: the thermal activation (TA) at 250 K > T > 130 K, the nearest-neighbor hopping (NNH) at 130 K > T > 60 K, and the variable-range hopping (VRH) below 60 K (sample A of $L = 3.6$ μm and $W =$ 1.5 μm, see Fig. 2f and Supplementary Fig. 7a and 7b). These transport regimes are consistent with previous studies[37,38]. Since pronounced nonlocal signals are observed in all three transport regimes, there appears no clear connection between the transport regimes and the onset of strong nonlocal signals. Interestingly, the characteristic temperatures of both NNH and VRH for R_{NL} are much larger than those for R_L in the range of $V_g \sim -60$ to -58 V (Supplementary Fig. 7d and 7e). This indicates a higher energy barrier in the nonlocal transport and an anomalous origin of the nonlocal signal.

To determine the origin of the observed R_{NL}, we investigate the scaling relation between R_{NL} and R_L as functions of V_g at different temperatures for both sample A (Fig. 2) and sample B (Supplementary Fig. 8). For a fixed V_g, both R_L and R_{NL} increase when the temperature is lowered. In sample A, two regimes with distinct scaling behaviors become clearly visible in Fig. 2c, d, the logarithmic plot of R_L and R_{NL} at different V_g. Above 160 K, the slopes of the lnR_{NL} versus lnR_L curves are 1, indicating that $R_{NL} \propto R_L$. Below 160 K, the slopes turn to 3 in the low electron density regime ($R_L \approx 10^8$ to $10^9\,\Omega$), which amounts to $R_{NL} \propto R_L^3$. Indeed, a diffusive model has predicted such power-law

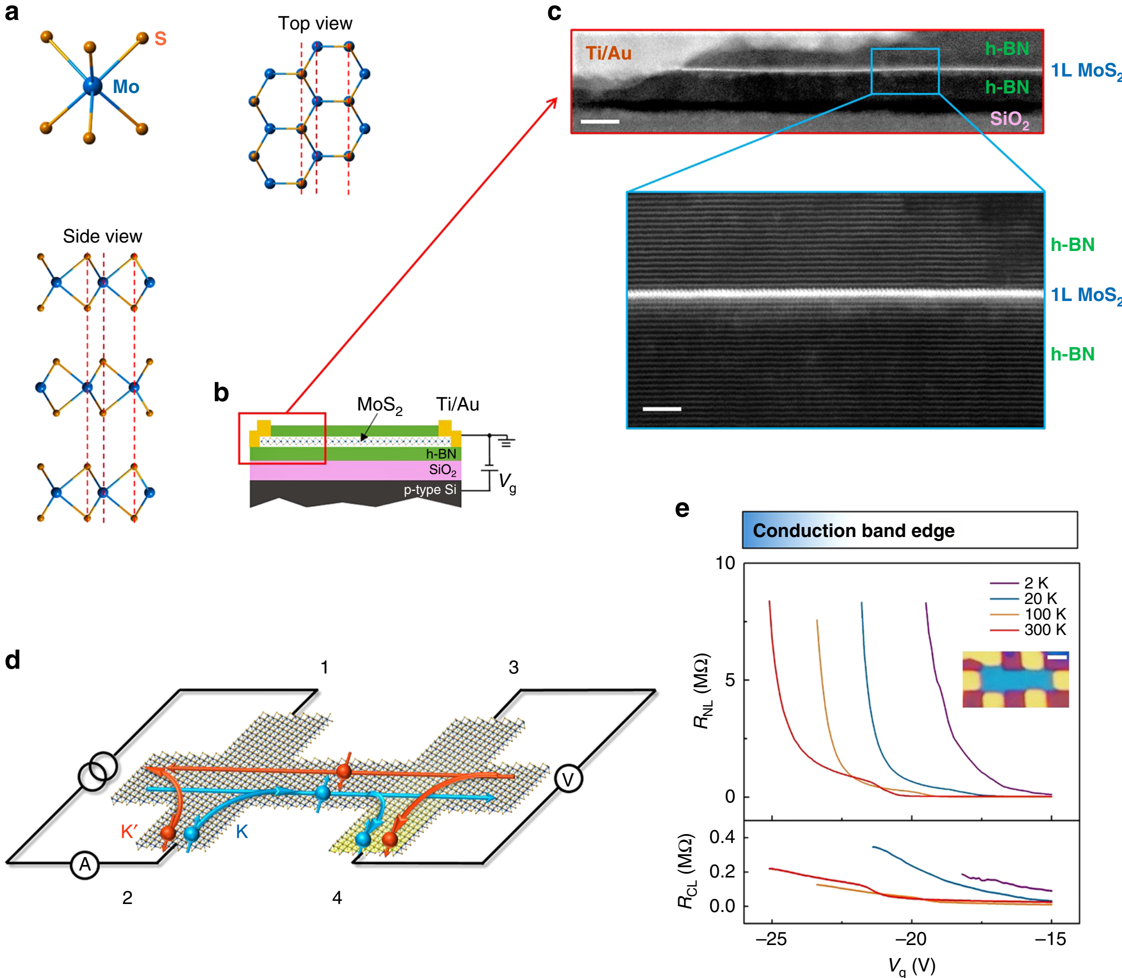

Fig. 1 Valley Hall transport induced nonlocal resistance in monolayer MoS_2. **a** Top view and side view of the crystal structure of 2H-MoS_2; an odd- (even-) layer is inversion asymmetric (symmetric). **b** Schematic of the h-BN encapsulated MoS_2 field-effect transistor. **c** High-resolution bright-field STEM image showing details of the edge-contacted monolayer MoS_2 device structure (scale bar 10 nm). The expanded region shows that the BN-MoS_2-BN interface is pristine and free of impurities down to the atomic scale (scale bar 3 nm). **d** Schematic of the nonlocal resistance measurement and the VHE-mediated nonlocal transport. The applied charge current in the left circuit generates a pure valley current in the transverse direction via a VHE. This valley current induces opposite chemical potential gradients for the two valleys over the inter-valley scattering length, which, in turn, generates a voltage drop measured by probes 3 and 4 in the right circuit via an inverse VHE. **e** Nonlocal resistance R_{NL} (upper panel) and the classical ohmic contribution R_{CL} (lower panel) as functions of gate voltage V_g at varied temperatures. Inset: optical image of a typical monolayer MoS_2 device (scale bar 2 μm). A MoS_2 Hall bar is sandwiched between the top and bottom h-BN flakes

relations[36], in which a cubic scaling holds for a spin or valley Hall effect[36]. As introduced above and calculated later, the massive Dirac band structure of monolayer MoS_2 produces large valley Hall conductivity σ_{xy}^{V} (see below) but much weaker spin Hall conductivity[36] (see Supplementary Note 1), Therefore, it is natural to attribute the observed nonlocal signal to the VHE, and the obtained cubic scaling may be analyzed by the predicted formula[36]

$$R_{NL} = \frac{1}{2}\left(\frac{\sigma_{xy}^{V}}{\sigma_{xx}}\right)^2 \frac{W}{\sigma_{xx} l_V} e^{-\frac{L}{l_V}} \propto \left(\sigma_{xy}^{V}\right)^2 R_L^3. \quad (1)$$

where l_V is the valley diffusion length (or inter-valley scattering length), and σ_{XX} and R_L have the simple relation of $\sigma_{xx} = \frac{L}{R_L W}$. We will focus on such a VHE-based hypothesis now and elaborate more on the exclude of spin Hall effect in Discussion.

The R_{NL} and R_L data measured at different temperatures for the case of $V_g = -60$ V are plotted in Fig. 2d. The cubic law is not applicable above 160 K, due to the enhancement of inter-valley scattering by the smear of the lowest conduction sub-band spin splitting (estimated as $E_s/k_B \sim 169$ K, see Supplementary Fig. 9) at high temperatures. Below 160 K, Eq. (1) can be employed to estimate l_V. For the case of intermediate inter-valley scattering and edge roughness, $l_V \sim 0.36$ μm if we assume $\sigma_{xy}^{V} \sim 1e^2/h$. In the limit of strong inter-valley scattering and edge roughness, $l_V \sim 0.43$ μm if we assume $\sigma_{xy}^{V} \sim 0.1e^2/h$. These values of l_V are comparable to those obtained in graphene systems[10–14,17,18].

We further investigated the length dependence of the nonlocal valley transport. Apart from sample A ($L = 3.6$ μm) and sample B ($L = 6$ μm), two more samples ($L = 11$ μm and 16 μm) are investigated (Supplementary Fig. 8). The semilog plot of R_{NL} at $n = 4 \times 10^{11}$ cm^{-2} (extracted from the Hall measurement, see Supplementary Fig. 10) versus the sample length yields an estimate of $l_V \sim 1$ μm (Fig. 2g). This value is very close to W and much larger than the electron mean-free path $l_m \sim 20$ nm (estimated from the sample mobility μ for the range of n where the cubic scaling appears) and the localization length $\xi \sim 50$ nm

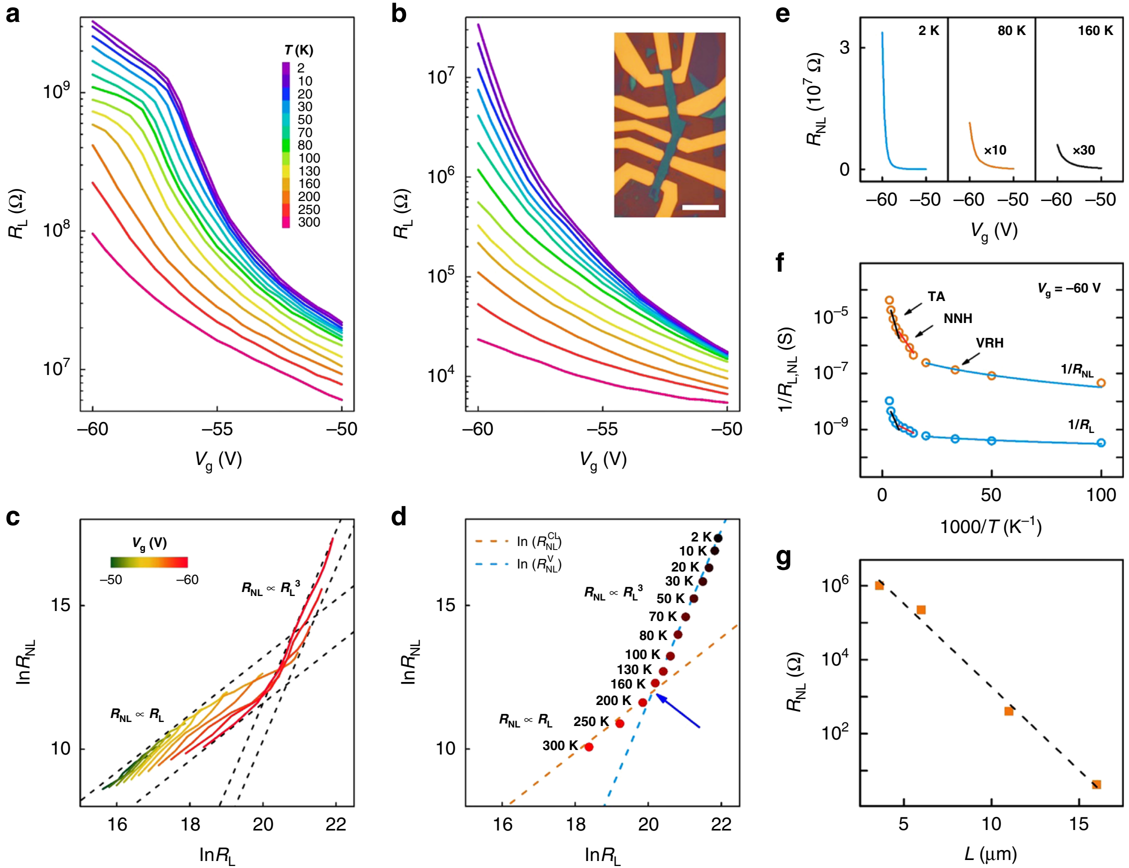

Fig. 2 Local and nonlocal resistances of monolayer MoS_2. **a**, **b** Semilog plots of R_L and R_{NL} as a function of V_g measured at varied temperatures. Inset of **b**: optical micrograph of our typical h-BN/MoS_2/h-BN device with multi-terminal Hall Bar configurations. Scale bar: 5 μm. **c** Scaling relations between ln R_L and ln R_{NL} at V_g ranging from −50 V to −60 V. When the electron density is relatively high, i.e., R_L and R_{NL} are small, R_{NL} is linearly proportional to R_L. When the electron density is relatively low, a crossover from linear to cubic scaling is observed. The critical density $nc = 4 \times 10^{11}$ cm^{-2}, with the gate voltage $V_g = -57$ V. **d** Crossover phenomenon by considering classical diffusion ($R_{NL} \propto R_L$) and valley Hall transport ($R_{NL} \propto R_L{}^3$). The experimental data (solid circles, $V_g = -60$ V) clearly show two different regimes which are fitted by two linear curves (orange dashed line with slope 1 and blue dashed line with slope 3). The critical temperature is around 160 K~200 K, as marked by the blue arrow. **e** R_{NL} plotted as a function of V_g at low temperatures. The ohmic contribution, calculated according to R_L and device geometry, is deducted from the measured R_{NL} at different temperatures. **f** $1/R_{NL}$ (orange circles) and $1/R_L$ (blue circles) in log scale plotted as functions of $1/T$ at $V_g = -60$ V. Three distinct transport regimes were observed: the thermal activation (TA) transport, nearest neighbor hopping (NNH) transport, and the variable range hopping (VRH) transport. **g** Semilog plot of R_{NL} as a function of L at $n = 2 \times 10^{11}$ cm^{-2} (orange squares). Nonlocal signal decays exponentially with increasing L. The dashed line yields a valley diffusion length of ~1 μm

(see Supplementary Fig. 11). Nevertheless, these estimates based on the observed nonlocal signals are suggestive of l_v in the order of micron. In sample B, the cubic scaling remains even at room temperature, attributed to the dominant valence-band contribution to σ_{xy}^V and particularly the large intrinsic bandgap that is impossible for graphene systems.

Nonlocal transport in bilayer and trilayer MoS_2. For bilayer MoS_2, the measured R_L and R_{NL} as functions of V_g at different temperatures are plotted in Fig. 3a, b. As the carrier density increases, R_L and R_{NL} decrease in a similar fashion in the temperature range of 5–50 K. This yields a linear scaling behavior between R_L and R_{NL}, as analyzed in Fig. 3c, d, and no cubic scaling is detected. We note that extrinsic P symmetry breaking can be introduced into atomically thin bilayers via external gating, as achieved in bilayer graphene[11,12], and that detecting a nonlocal signal in gated bilayer graphene requires a threshold gating strength[11,12]. In our devices, however, V_g is too low to reach the threshold estimated by an recent optical experiment[18], the estimated potential difference between the top and bottom layers is ~ 9.2 meV at $V_g = -60$ V. This weak symmetry breaking produces little change in the total Berry curvature as compared with the pristine case (Supplementary Fig. 12), given the facts that the induced potential is much smaller than the bandgap and that the valence-band contribution to σ_{xy}^V is dominant. In light of this analysis, the gating-induced P symmetry breaking is negligible in our bilayer MoS_2. Therefore, we conclude that the absence of cubic scaling in bilayer MoS_2 indicates the crucial role of strong P symmetry breaking in generating VHE. This is consistent with the theoretical understanding of VHE[5–9], as aforementioned in Introduction.

This key conclusion can be immediately tested in thicker MoS_2 samples. Given that P symmetry is broken (respected) in pristine odd-layer (even-layer) MoS_2, one might wonder whether the intrinsic VHE and its cubic scaling could be detected in trilayer MoS_2. Figure 3e, f display our R_L and R_{NL} data measured in trilayer MoS_2 as functions of V_g at different temperatures. Evidently, the measured R_{NL} rapidly decreases as V_g increases in the narrow range of $-20\ \mathrm{V} < V_g < -18.4$ V, which is reminiscent of the behavior of R_{NL} in our monolayer devices in the low density regime. Similar to the monolayer case, the logarithmic

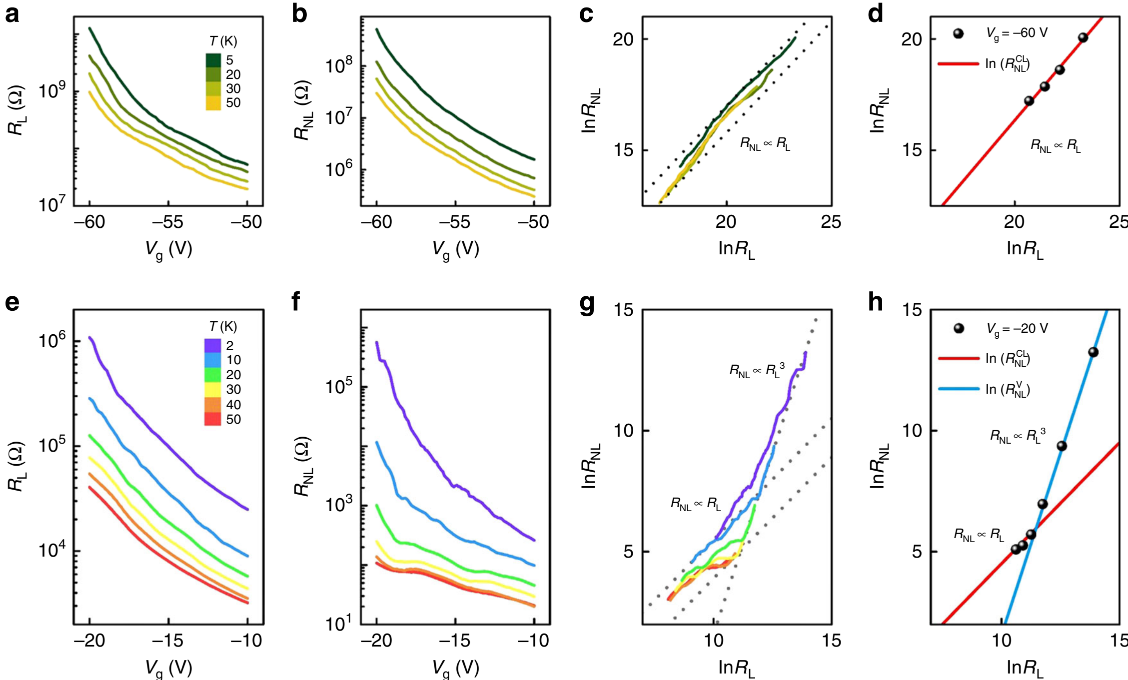

Fig. 3 Local and nonlocal resistances of bilayer and trilayer MoS_2. **a**, **b**, **e**, **f** Gate-dependence of R_L and R_{NL} at different temperatures in bilayer **a**, **b** and trilayer **e**, **f** samples. **c**, **g** Scaling relation between ln R_L and ln R_{NL} is obtained at different temperatures in bilayer **c** and trilayer **g** samples. For the trilayer case, R_{NL} scales linearly with R_L in the high electron density regime, whereas the cubic scaling law $R_{NL} \propto R_L{}^3$ is observed in the low electron density regime ($nc = 4 \times 10^{11}$ cm^{-2} or $V_g = -18.4$ V). **d** lnR_L v.s. lnR_{NL} for bilayer MoS_2. In the full range of gate voltages, R_{NL} scales linearly with R_L, and the experimental data (black dots, $V_g = -60$ V) is fitted by a linear curve (red solid line). **h** lnR_L v.s. lnR_{NL} for trilayer MoS_2. The experimental data (black dots, $V_g = -20$ V) clearly show two different regimes which are fitted by two linear curves (red solid line with slope 1 and blue solid line with slope 3). Evidently, a crossover exists from linear ($R_{NL} \propto R_L$) to cubic scaling behaviors ($R_{NL} \propto R_L{}^3$)

plots of R_L and R_{NL} in Fig. 3g exhibit clear changes in slop from 1 to 3 near $V_g = -18.4$ V, further confirming the observation of the nonlocal signal of VHE in trilayer MoS_2. To illustrate the temperature dependence, Fig. 3h plots the scaling relation between R_L and R_{NL} at different temperatures for the case of $V_g = -20$ V. Again, there is a clear change in slop from 1 to 3 near 30 K. Moreover, the valley diffusion length can be extracted based on Fig. 3h and Eq. (1). We obtain $l_V \sim 0.5$ μm and ~1 μm, respectively, for the aforementioned two limits $\sigma_{xy}^V \sim 1e^2/h$ and $\sim 0.1\ e^2/h$. Both the observed amplitude of nonlocal signal and the estimated valley diffusion length in the trilayer MoS_2 devices are comparable to those in the monolayer case. In addition to the crucial role of P symmetry breaking, significantly, these observations are suggestive of a universal physical origin of VHEs in odd-layer TMDCs, as discussed below.

Layer-dependent Berry curvatures. To better understand the thickness dependent observations, we calculate the electronic band structures and Berry curvatures[15,16] for monolayer, bilayer, and trilayer MoS_2. The band structures in Fig. 4a, c are indeed thickness dependent. In particular, the conduction-band minima lie at the K-valleys for the monolayer, whereas they shift to the Q-valleys for the bilayer and trilayer. Given the low electron densities in our samples ($\sim 4 \times 10^{11}$ cm^{-2} in monolayers and trilayers, $\sim 1 \times 10^{12}$ cm^{-2} in bilayers), the Fermi levels only cross the lowest conduction sub-bands, as indicated by the green lines in Fig. 4a, c. As bilayer MoS_2 has a restored P symmetry that is intrinsically broken in odd-layer MoS_2, the sub-bands are spin degenerate in the bilayer yet spin split in the monolayer and trilayer. With these band structures, we further compute the Berry curvatures that drive the VHEs. Berry curvature vanishes if both P and T are present. As plotted in Fig. 4d, f, our calculations reveal that the curvatures are indeed trivial in the bilayer yet substantial in the monolayer and trilayer. This explains the reason why no cubic scaling is observed in bilayer MoS_2 and highlights the role of P symmetry breaking in producing VHEs.

It is puzzling to understand and compare the nonlocal signals of VHEs in monolayer and trilayer MoS_2. Similar cubic scaling behaviors and their transitions to linear ones above the critical densities or temperatures are observed in both cases. However, the conduction-band Berry curvatures (the difference between the blue and orange curves in Fig. 4d, f) are large in the monolayer K-valleys yet negligibly small in the trilayer Q-valleys. This implies that the geometric explanation of VHE requiring finite doping[5] should not be the origin[11], which is further evidenced by the fact that the cubic scaling behaviors weaken rapidly with increasing the electron densities.

On the other hand, these facts appear to be in harmony with the topological VHE[6–9] that arises from the valley Hall conductivity (see Supplementary Note 1). This conductivity amounts to the total valley-contrasting Berry curvature contributed from all occupied states, i.e., all the states below the Fermi level if at zero temperature. In our case, the monolayer and trilayer share almost identical substantial valence-band Berry curvatures (the orange curves in Fig. 4d, f), due to the extremely weak interlayer couplings. By contrast, the conduction-band contributions are different but very minor (the difference between the blue and orange curves in Fig. 4d, f) because of the low electron densities. Therefore, the valence-band contributions dominate the valley Hall conductivities, leading to similar nonlocal signals of VHEs in monolayer and trilayer. Recently, nearly quantized edge transports have been observed along the designed or selected domain walls in graphene systems[13,14] and

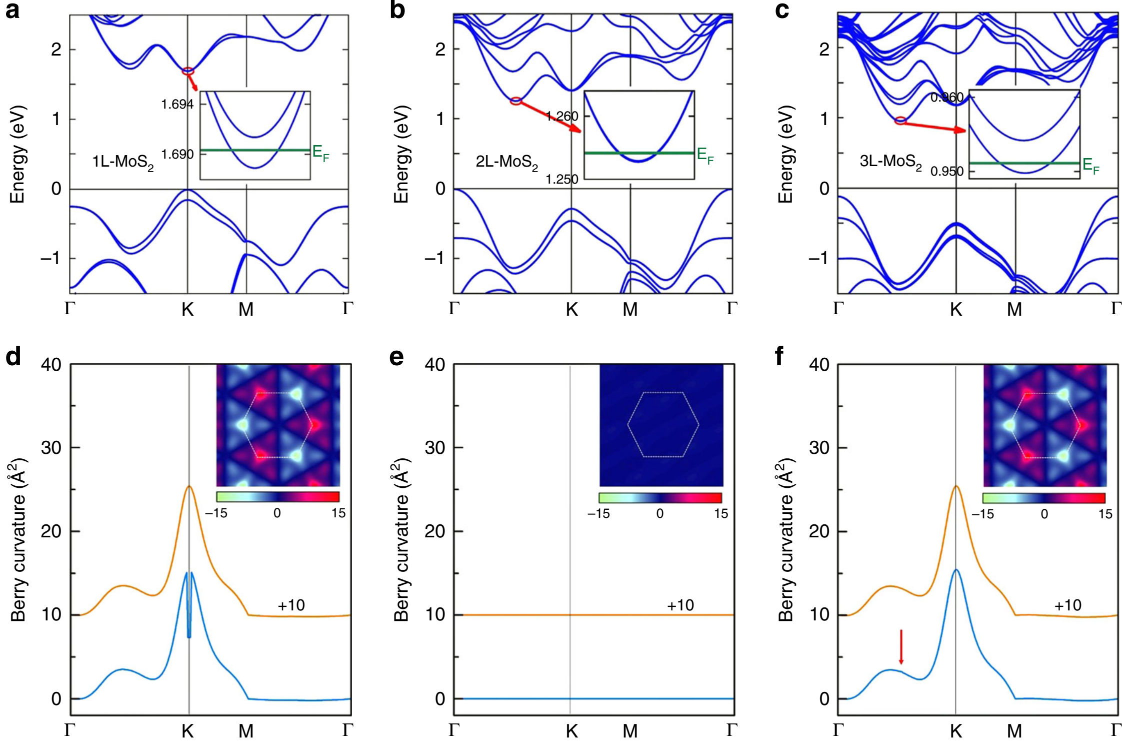

Fig. 4 Band structures and Berry curvatures of atomically thin MoS_2. **a**–**c** Band structure of (**a**) monolayer, (**b**) bilayer, and (**c**) trilayer MoS_2. The conduction band edges lie at the K-valleys in the monolayer but at the Q-valleys in the bilayer and trilayer. Insets of **a**–**c**: The Fermi levels only cross the lowest sub-bands, which are spin degenerate in **b** but spin split in **a** and **c**. **d**–**f** Berry curvatures of **d** monolayer, **e** bilayer, and **f** trilayer MoS_2. The blue curves are the total curvatures of all occupied states below the Fermi levels (~2 meV from the conduction band bottom), whereas the orange curves are the total curvatures of all valence-band states. The red arrow in **f** points out a tiny bump at a Q-valley. Insets of **d**–**f** 2D mapping of Berry curvatures in the 2D Brillouin zone (white dashed lines)

even in artificial crystals[19]. In our case, the roughness of natural edges can cause edge inter-valley scattering[8] and remove any possible edge state[39]. This also partly reduces the valence-band contributions[4] which in principle would result in a quantized valley Hall conductivity (valley Chern number[6,8]) in the massive Dirac model.

Discussion

Finally, we note that the VHE and spin Hall effects are distinct in TMDCs, in spite of the spin-valley locking. The spin-valley locking is a property at Fermi level only when it lies in the lowest conduction or highest valence sub-band. Yet, all states below Fermi level contribute to the spin and valley Hall conductivities[6] (see Supplementary Note 1). Although a similar line of analysis based on Eq. (1) can be done for a theoretical hypothesis of spin Hall effect as well, it appears that this is not the case for three reasons. First, the spin Hall conductivities are predicted to be very small for pristine odd-layer TMDCs when the valence bands are fully filled[16] (see Supplementary Note 1). Second, the observed nonlocal resistances have little response to a magnetic field up to 9 T (Supplementary Fig. 13). Third, the spin diffusion length in TMDCs is at the scale of several tens of nanometers[40,41], which is 1–2 orders smaller than the extracted diffusion lengths based on our experimental data or Eq. (1).

In conclusion, the pronounced nonlocal signals are observed in our MoS_2 samples with length up to 16 μm and at temperature up to 300 K. The valley diffusion lengths are also estimated to be in the order of micron. The low carrier concentration ensures the low possibility of bulk inter-valley scattering and maintains a long valley diffusion length. In addition, the mirror and T symmetries lock the spin and valley indices of the lowest sub-bands, preventing bulk inter-valley scattering via spin conservation. Our observed intrinsic VHEs and their long valley diffusion lengths are promising for realizing room-temperature low-dissipation valleytronics. To better elucidate the outstanding problems of both geometric[5] and topological[6–9] VHEs, our observations and analyses call for future efforts, particularly complementary experiments in p-type TMDCs (where spin Hall conductivities are predicted to be much larger[16]) such as the one[42] that we became aware of during the peer review process.

Methods

Van der Waals structures. MoS_2 bulk crystals are bought from 2D semiconductors (website: http://www.2dsemiconductors.com/), and the h-BN sources (grade A1) are bought from HQ graphene (website: http://www.hqgraphene.com/). To fabricate van der Waals heterostructures, a selected MoS_2 sample is picked from the SiO_2/Si substrate by a thin h-BN flake (5–15 nm thick) on PMMA (950 A7, 500 nm) via van der Waals interactions. The h-BN/MoS_2 flake is then transferred onto a fresh thick h-BN flake lying on another SiO_2/Si substrate, to form a BN-MoS_2-BN heterostructure (step 1 in Supplementary Fig. 1).

Layer numbers and stacking orders. To determine the number of layers for a MoS_2 sample, we carried out micro-Raman and photoluminescence measurements before making a device (Supplementary Fig. 14). We also took cross-sectional STEM (JEOL JEM-ARM200F Cs-corrected TEM, operating at 60 kV) images after the electronic measurement. The STEM image can clearly determine the number of MoS_2 layers (Supplementary Fig. 14) and distinguishes the 2H stacking order from other stacking orders such as 1T and 3R (Supplementary Fig. 15).

Selective etching process. A hard mask is patterned on the heterostructure by the standard e-beam lithography technique using PMMA (step 2 in Supplementary Fig. 1). The exposed top BN layer and MoS_2 are then etched via reactive ion etching (RIE), forming a Hall bar geometry (steps 3 & 4 in Supplementary Fig. 1). Then a second-round e-beam lithography and RIE is carried out to expose the MoS_2 layer (steps 5 & 6 in Supplementary Fig. 1). The electrodes are then patterned by a third-round e-beam lithography followed by a standard e-beam evaporation (steps 7 & 8

in Supplementary Fig. 1). To access the conduction band edges of MoS_2, we choose Titanium as the contact metal, as the work function of Titanium (~4.3 eV) matches the band-edge energy of MoS_2 (~4.0–4.4 eV depending on the layer numbers).

Electronic measurement. The $I–V$ curves are measured by Keithley 6430. Other transport measurements are carried out by using: (i) low-frequency lock-in technique (SR 830 with SR550 as the preamplifier and DS 360 as the function generator, or (ii) Keithley 6430 source meter (>10^{16} Ω input resistance on voltage measurements). The cryogenic system provides stable temperatures ranging from 1.4 to 300 K. A detailed discussion of the nonlocal measurement is presented in Supplementary Fig. 6.

Data availability

The authors declare that the major data supporting the findings of this study are available within the paper and its Supplementary Information. Extra data are available from the authors upon reasonable request.

Received: 24 April 2018 Accepted: 23 January 2019
Published online: 05 February 2019

References

1. Gunawan, O. et al. Valley susceptibility of an interacting two-dimensional electron system. *Phys. Rev. Lett.* **97**, 186404 (2006).
2. Gunawan, O., Habib, B., De Poortere, E. P. & Shayegan, M. Quantized conductance in an AlAs two-dimensional electron system quantum point contact. *Phys. Rev. B* **74**, 155436 (2006).
3. Rycerz, A., Tworzydlo, J. & Beenakker, C. W. J. Valley filter and valley valve in graphene. *Nat. Phys.* **3**, 172–175 (2007).
4. Zhang, F. Brought to light. *Nat. Phys.* **14**, 111–113 (2018).
5. Xiao, D., Yao, W. & Niu, Q. Valley-contrasting physics in graphene: magnetic moment and topological transport. *Phys. Rev. Lett.* **99**, 236809 (2007).
6. Zhang, F., Jung, J., Fiete, G. A., Niu, Q. & MacDonald, A. H. Spontaneous quantum Hall states in chirally stacked few-layer graphene systems. *Phys. Rev. Lett.* **106**, 156801 (2011).
7. Martin, I., Blanter, Y. M. & Morpurgo, A. F. Topological confinement in bilayer graphene. *Phys. Rev. Lett.* **100**, 036804 (2008).
8. Zhang, F., MacDonald, A. H. & Mele, E. J. Valley Chern numbers and boundary modes in gapped bilayer graphene. *Proc. Natl. Acad. Sci.* **110**, 10546–10551 (2013).
9. Vaezi, A., Liang, Y., Ngai, D. H., Yang, L. & Kim, E.-A. Topological edge states at a tilt boundary in gated multilayer graphene. *Phys. Rev. X* **3**, 021018 (2013).
10. Gorbachev, R. V. et al. Detecting topological currents in graphene superlattices. *Science* **346**, 448–451 (2014).
11. Sui, M. et al. Gate-tunable topological valley transport in bilayer graphene. *Nat. Phys.* **11**, 1027–1031 (2015).
12. Shimazaki, Y. et al. Generation and detection of pure valley current by electrically induced Berry curvature in bilayer graphene. *Nat. Phys.* **11**, 1032–1036 (2015).
13. Ju, L. et al. Topological valley transport at bilayer graphene domain walls. *Nature* **520**, 650–655 (2015).
14. Li, J. et al. Gate-controlled topological conducting channels in bilayer graphene. *Nat. Nanotechnol.* **11**, 1060–1065 (2016).
15. Xiao, D., Liu, G., Feng, W., Xu, X. & Yao, W. Coupled spin and valley physics in monolayers of MoS_2 and other group-VI dichalcogenides. *Phys. Rev. Lett.* **108**, 196802 (2012).
16. Li, X., Zhang, F. & Niu, Q. Unconventional quantum Hall effect and tunable spin Hall effect in Dirac materials: Application to an isolated MoS_2 trilayer. *Phys. Rev. Lett.* **110**, 066803 (2013).
17. Mak, K. F., McGill, K. L., Park, J. & McEuen, P. L. The valley Hall effect in MoS_2 transistors. *Science* **344**, 1489–1492 (2014).
18. Lee, J., Mak, K. F. & Shan, J. Electrical control of the valley Hall effect in bilayer MoS_2 transistors. *Nat. Nanotechnol.* **11**, 421–425 (2016).
19. Lu, J. et al. Observation of topological valley transport of sound in sonic crystals. *Nat. Phys.* **13**, 369–374 (2017).
20. Mak, K. F., He, K., Shan, J. & Heinz, T. F. Control of valley polarization in monolayer MoS_2 by optical helicity. *Nat. Nanotechnol.* **7**, 494–498 (2012).
21. Zeng, H., Dai, J., Yao, W., Xiao, D. & Cui, X. Valley polarization in MoS_2 monolayers by optical pumping. *Nat. Nanotechnol.* **7**, 490–493 (2012).
22. Cao, T. et al. Valley-selective circular dichroism of monolayer molybdenum disulphide. *Nat. Commun.* **3**, 887 (2012).
23. Mak, K. F., Lee, C., Hone, J., Shan, J. & Heinz, T. F. Atomically thin MoS2: a new direct-gap semiconductor. *Phys. Rev. Lett.* **105**, 136805 (2010).
24. Splendiani, A. et al. Emerging photoluminescence in monolayer MoS_2. *Nano. Lett.* **10**, 1271–1275 (2010).
25. Cui, X. et al. Multi-terminal transport measurements of MoS_2 using a van der Waals heterostructure device platform. *Nat. Nanotechnol.* **10**, 534–540 (2015).
26. Movva, H. C. P. et al. High-mobility holes in dual-gated WSe_2 field-effect transistors. *ACS Nano* **9**, 10402–10410 (2015).
27. Shuigang, X. et al. Universal low-temperature Ohmic contacts for quantum transport in transition metal dichalcogenides. *2D Mater.* **3**, 021007 (2016).
28. Wu, Z. et al. Even-odd layer-dependent magnetotransport of high-mobility Q-valley electrons in transition metal disulfides. *Nat. Commun.* **7**, 12955 (2016).
29. Pisoni, R. et al. Gate-defined one-dimensional channel and broken symmetry states in MoS_2 van der waals heterostructures. *Nano. Lett.* **17**, 5008–5011 (2017).
30. Lin, J. et al. Probing Landau levels of strongly interacting massive dirac electrons in layer-polarized MoS_2. https://arxiv.org/abs/1803.08007 (2018).
31. Larentis, S. et al. Large effective mass and interaction-enhanced Zeeman splitting of K-valley electrons in $MoSe_2$. *Phys. Rev. B* **97**, 201407 (2018).
32. Fallahazad, B. et al. Shubnikov-de haas oscillations of high-mobility holes in monolayer and bilayer WSe_2: Landau level degeneracy, effective mass, and negative compressibility. *Phys. Rev. Lett.* **116**, 086601 (2016).
33. Movva, H. C. P. et al. Density-dependent quantum hall states and zeeman splitting in monolayer and bilayer WSe_2. *Phys. Rev. Lett.* **118**, 247701 (2017).
34. Gustafsson, M. V. et al. Ambipolar Landau levels and strong band-selective carrier interactions in monolayer WSe_2. *Nat. Mater.* **17**, 411 (2018).
35. Xu, S. et al. Odd-integer quantum hall states and giant spin susceptibility in p-type few-layer WSe_2. *Phys. Rev. Lett.* **118**, 067702 (2017).
36. Abanin, D. A., Shytov, A. V., Levitov, L. S. & Halperin, B. I. Nonlocal charge transport mediated by spin diffusion in the spin Hall effect regime. *Phys. Rev. B* **79**, 035304 (2009).
37. Qiu, H. et al. Hopping transport through defect-induced localized states in molybdenum disulphide. *Nat. Commun.* **4**, 2642 (2013).
38. Lo, S.-T. et al. Transport in disordered monolayer MoS2 nanoflakes—evidence for inhomogeneous charge transport. *Nanotechnology* **25**, 375201 (2014).
39. Wu, D. et al. Uncovering edge states and electrical inhomogeneity in MoS_2 field-effect transistors. *Proc. Natl. Acad. Sci.* **113**, 201605982 (2016).
40. Wang, L. & Wu, M. Electron spin diffusion in monolayer MoS 2. *Phys. Rev. B* **89**, 205401 (2014).
41. Sinova, J., Valenzuela, S. O., Wunderlich, J., Back, C. & Jungwirth, T. Spin hall effects. *Rev. Mod. Phys.* **87**, 1213 (2015).
42. Fallahazad, B. M. et al. Spin hall effect in monolayer and bilayer WSe_2. *APS March Meet.* **L49**, 002 (2017). abstract id.

Acknowledgements

We acknowledge the financial support from the Research Grants Council of Hong Kong (Project Nos. 16300717, 16302215, 16324216, C7036-17W, C6026-16W, and HKUST3/CRF13G), the Croucher Foundation, the Dr. Taichin Lo Foundation, the National Key R&D Program of China (with grant number 2017YFB0701600), US Army Research Office (under grant number W911NF-18-1-0416), and UT-Dallas Research Enhancement Funds. We acknowledge the technical support from Wing Ki Wong and the Raith–HKUST Nanotechnology Laboratory at MCPF. Z.W. acknowledges useful conversations with Danru Qu. F.Z. is grateful to Allan MacDonald, Joe Qiu, and Di Xiao for valuable discussions.

Author contributions

Z.W. and N.W. conceived and designed the experiments. F.Z. provided the theoretical support. N.W. and F.Z. supervised the work. Z.W. fabricated the devices, performed the measurements, and analyzed the data with the help from M.H., J.L., T.H., L.A., Y.W., S.X., G.L., C.C. and K.T.L. X.C. carried out the STEM characterizations. G.-B.L. computed the band structures and Berry curvatures. F.Z. and P.C. analyzed the band structures and Berry curvatures and provided theoretical explanations. Z.W., F.Z., B.T.Z. and N.W. wrote the manuscript with contributions from all authors.

Additional information

Supplementary Information accompanies this paper at https://doi.org/10.1038/s41467-019-08629-9.

Competing interests: The authors declare no competing interests.

Reprints and permission information is available online at http://npg.nature.com/reprintsandpermissions/

Journal peer review information: *Nature Communications* thanks the anonymous reviewers for their contribution to the peer review of this work.

Publisher's note: Springer Nature remains neutral with regard to jurisdictional claims in published maps and institutional affiliations.

Open Access This article is licensed under a Creative Commons Attribution 4.0 International License, which permits use, sharing, adaptation, distribution and reproduction in any medium or format, as long as you give appropriate credit to the original author(s) and the source, provide a link to the Creative Commons license, and indicate if changes were made. The images or other third party material in this article are included in the article's Creative Commons license, unless indicated otherwise in a credit line to the material. If material is not included in the article's Creative Commons license and your intended use is not permitted by statutory regulation or exceeds the permitted use, you will need to obtain permission directly from the copyright holder. To view a copy of this license, visit http://creativecommons.org/licenses/by/4.0/.

© The Author(s) 2019